Magnetic behavior of 3D interconnect nanoporous FeCo synthesized by liquid metal dealloying

Benjamin Ducharne, Jae-Hyuk Lee, Soo-Hyun Joo, Pierre-Antoine Geslin, Eric Wasniewski, Hidemi Kato

Magnetic behavior of 3D interconnect nanoporous FeCo synthesized by liquid metal dealloying

Benjamin Ducharne[1,2], Jae-Hyuk Lee[3], Soo-Hyun Joo[3], Pierre-Antoine Geslin[4], Eric Wasniewski[5,6,7] and Hidemi Kato[8]

[1]ELyTMaX IRL3757, CNRS, Univ. Lyon, INSA Lyon, Centrale Lyon, Université Claude Bernard Lyon 1, Tohoku University, Sendai, Japan, benjamin.ducharne@insa-lyon.fr

[2]Univ. Lyon, INSA-Lyon, LGEF EA682, F69621, France

[3]Department of Materials Science and Engineering, Dankook University, 119 Dandae–ro, Cheonan 31116, Republic of Korea

[4]CNRS, INSA Lyon, Universite Claude Bernard Lyon 1, MATEIS, UMR5510, 69621 Villeurbanne, France

[5]Cetim, 52 avenue Félix Louat 60300 Senlis, France

[6]Université Paris-Saclay, CentraleSupélec, CNRS, Laboratoire de Génie Électrique et Électronique de Paris, 91192, Gif-sur-Yvette, France

[7]Sorbonne Université, CNRS, Laboratoire de Génie Électrique et Électronique de Paris, 75252, Paris, France

[8]Institute for Materials Research, Tohoku University, Sendai 980-8577, Japan

Abstract

Liquid Metal Dealloying (LMD) is tested to enhance the near-surface magnetic properties of ferromagnetic Iron-Cobalt alloys. With a lower surface electrical conductivity, treated specimens are expected to accommodate the frequency effect better and exhibit a lower level of magnetic loss. This work focuses on the magnetic viability of LMD-treated samples. The magnetic hysteresis cycles of virgin, fully-dealloyed, and partially-dealloyed specimens are measured from quasi-static to dynamic regimes. For each category of specimens, experimental results are compared with numerical predictions given by dedicated hysteresis models. The simulation parameters of the fully-dealloyed and the virgin specimens are leveraged to predict the partially-dealloyed specimen's behavior and estimate the thickness of the treated area accurately and non-destructively. Together with SEM observations and finite element simulations, these results show that the magnetic behavior of the metallic part in the dealloyed layer is barely affected by the specimen porosity, but the average variations observed experimentally are primarily due to the distortion of the magnetic lines and changes in the local geometry.

Keywords

Liquid metal dealloying, non-destructive testing, surface treatment, magnetic behavior.

1 - Introduction

Liquid Metal Dealloying (LMD) is a process in which one or more components of a metallic alloy are selectively removed from a precursor alloy upon its immersion in a liquid metal bath, leaving behind a porous structure [1, 2]. This process is also referred to as selective leaching or selective dissolution. The elaboration of porous structures through LMD involves four stages: (i) elaboration of a precursor alloy, (ii) immersion into a liquid metal that selectively dissolves one component, (iii) solidification of the liquid metal leading to the formation of a composite microstructure, (iv) selective etching of one of the phases to obtain porous structures. The success of LMD depends on carefully selecting the original alloy composition, the liquid metal, and the desired properties of the resulting porous structure for a specific application [3-5]. LMD is versatile, as tuning the parameters (composition of the precursor and the melt, dealloying time and temperature, etc.) allows to control the resulting porous microstructure.

LMD is already envisioned as a promising elaboration process for specific applications, including catalysis, sensing, electrochemical applications, and biomedical devices [6-8]. There is one field, though, where LMD could be used to improve materials properties, but almost no investigation has been done so far: the electromagnetic energy conversion domain [9]. By changing the local properties near the surface, one can expect LMD to create magnetic laminations with enhanced properties that could enforce the limit of traditional magnetic cores. Surface treatments for improved magnetic properties already exist but consistently undergo a diffusive process rather than a dealloying one. Electrical steel lamination with high silicon content is a good illustration: silicon is diffused along the surface of the sample, which increases locally the electrical resistivity and reduces the overall magnetic power loss [10-12].

In [13], authors dealloyed ingots of $(FeCo)_{\alpha}Ni_{1-\alpha}$ by removing the nickel element, leaving behind a nanoporous structure made of FeCo. FeCo alloys are well-identified in the electromagnetic energy conversion community, and interest in them is increasing [14-16]. Permendur is the most known; it comprises 49% cobalt, 49% iron, and 2% vanadium [17]. Permendur is characterized by exciting magnetic properties, including, for the most significant, a very high saturation flux density, a low coercivity, and reduced core losses. Permendur high saturation level allows the resulting magnetic core to function at higher field strengths so that the core can be smaller and lighter for a given magnetic flux and power level. Permendur laminations are, for example, used for magnetic cores and pole pieces in lightweight aircraft transformers and electric motors [18].

A higher saturation level is an excellent way to increase the power density, but it is not the only one. An increase in the working frequency gives similar results but is unfortunately associated with a rise in the magnetic losses. A higher working frequency induces eddy currents that not only convert the magnetic energy into heat directly in the magnetic core but confine the magnetic field on the edges of the magnetic laminations that are not fully exploited anymore [19-21]. The solution proposed in [13] is to use LMD to modify the edges of the FeCo alloy lamination so that the newly formed porous structure exhibits reduced local electrical conductivity and overall magnetic losses. LMD is a surface treatment well adapted to this application; by controlling

the treatment time, one can precisely adjust the dealloyed thickness and ensure a good balance between the lamination's magnetic and mechanical properties.

Once finished, it is complex to evaluate the thickness and the dealloying thickness non-destructively. Still, this information is mandatory to ensure that LMD was appropriately achieved. The simulation methods described in this study can precisely reproduce the hysteresis cycles of virgin and fully-dealloyed specimens at different frequency levels and with a limited number of parameters. Then, the resulting virgin and fully-dealloyed configurations can be used to simulate a partially dealloyed specimen and return precisely the thickness of the LMD-treated part.

The objectives of this study are threefold; they include confirming that LMD is a valid way to modify the magnetic performances of FeCo alloys, observing and simulating the magnetic behavior of fully and partially porous LMD-treated specimens, and returning non-destructively using magnetic measurements and simulations, the dealloying depth. The latter objective and the associated conclusions are not restrictive to LMD but can be extended to any metal surface treatment. Those include shot-peening, carburizing, nitriding in structural steel parts (to make them harder and less vulnerable to wear issues), silicon diffusion in electrical steel (to make them more electrically resistive locally), etc.

2 – Tested specimens

2.1 – Precursor alloys

A button-shaped ingot of $(FeCo)_{70}Ni_{30}$, weighing approximately 40g, was created through arc melting, utilizing high-purity raw materials with a purity exceeding 99.9% in a purified Ar atmosphere [13]. The ingot underwent over four cycles of being turned over and re-melted to ensure chemical homogeneity. Subsequently, the button was cast into plate samples, each with a thickness of 4 mm, using an arc melting machine in conjunction with tilt casting. Following this, the plate samples underwent cold-rolling to achieve a thickness of 1.3 mm and were subjected to a 12-hour heat treatment at 1050 °C in a purified Ar atmosphere.

2.2 – LMD process

A metallic melt containing Mg-10at%Ca underwent inductive heating within a carbon crucible in a purified He atmosphere. The LMD process was carried out for 200 seconds at a constant temperature of 800 °C for the first category of specimens and 2 hours for the second.

The third category, called the "virgin" specimens, remained untreated. The raw materials, Mg and Ca, had purities of 99.9% and 99.5%, respectively. During the LMD process, only miscible Ni atoms in the precursor alloys were selectively dissolved into the Mg-10at%Ca melt. Simultaneously, Fe and Co atoms organized themselves into a 3D interconnected ligament structure through interface diffusion. Concurrently, Mg melt channels grew into the precursor alloy, demonstrating diffusion-coupled growth with the enriched immiscible solid phase. The LMD process resulted in a composite material featuring individually interconnected FeCo and Mg phases in a 3D structure. Subsequent etching in 1M acetic acid for 6 hours selectively removed the Mg phases. The selective dissolution of Ni results in the self-organization of Fe and Co atoms

into a 3D interconnected morphology. Fig. 1 depicts cross-sectional Scanning Electron Microscope (SEM) images of the partially treated specimen after the selective elimination of the Mg phase.

It is worth noting that the porosity of the dealloyed layer depends on the initial Ni concentration, and in our case, it was about 32%.

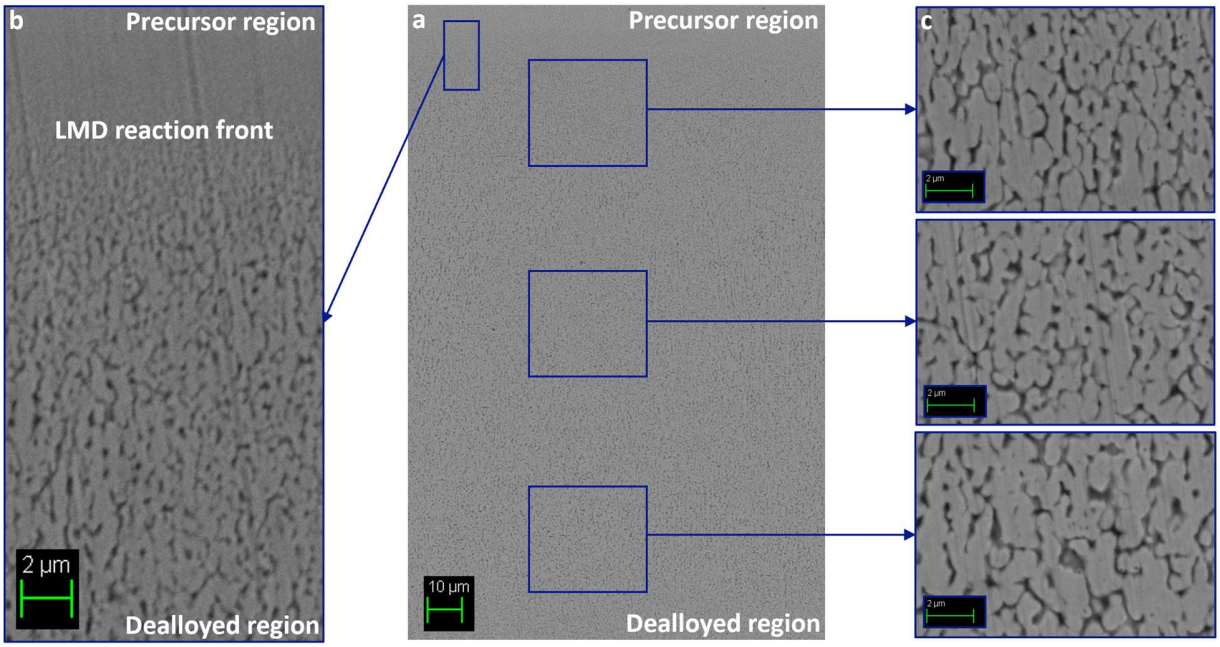

Fig. 1 – a Cross-sectional 3D interconnected nanoporous morphology observed by field emission scanning electron microscopy (FE-SEM). **Fig. 1 – b** Enlarged observation of the reaction front. **Fig. 1 – c** Enlarged observations of the dealloyed layer.

Fig. 1 – a reveals a sharp boundary between the dealloyed and the virgin segments. A narrow transition layer is noticeable (see Fig. 1 – b), and its thickness is minimal (approximately 2 µm). Far from the LMD reaction front (Fig. 1 – c), the microstructure looks relatively unchanged, with interconnections of FeCo and Mg-rich phases.

3 – Magnetic characterization setup

A dedicated test bench was designed to evaluate the average magnetic flux density B_a under the influence of a tangential surface excitation magnetic field H_{surf} at different frequency levels. A descriptive picture of the magnetic characterization setup is shown in Fig. 2:

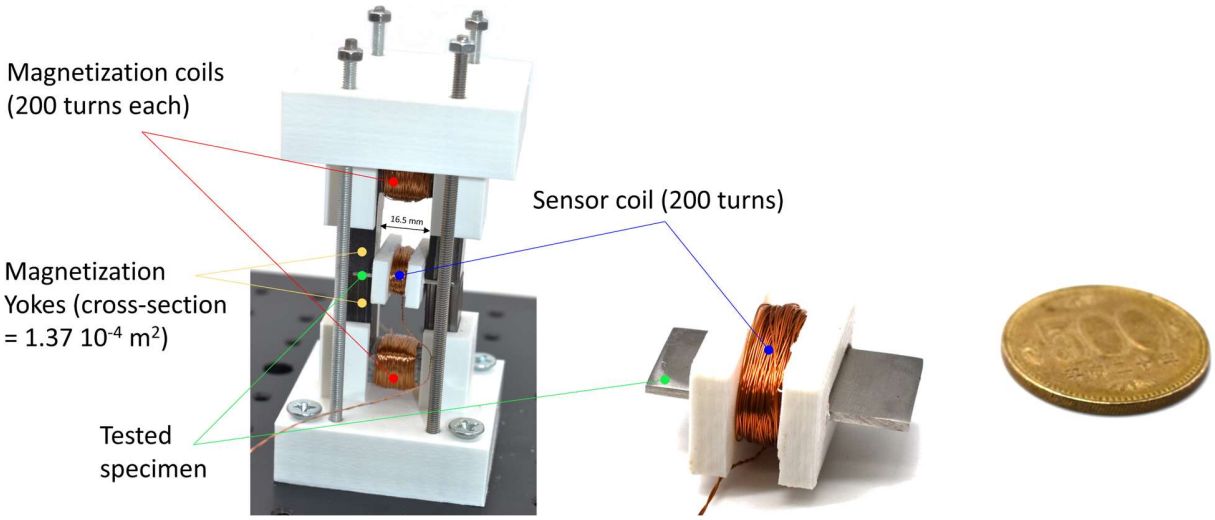

Fig. 2 – Descriptive photograph of the magnetic characterization setup.

The magnetization circuit comprised two oriented-grains electrical steel yokes and two N = 200-turn excitation coils connected in series. Each coil wrapped a yoke, as shown in Fig. 3. The cumulative cross-section of the yokes was worth 2.74 10^{-4} m^2, which is at least 14 times larger than the cross-section of the tested specimens. Considering this geometrical difference and the very high permeability of the oriented-grains electrical steel, one can assume the equivalent reluctance of the yokes as negligible and H_{surf} to be entirely confined in the tested specimens. The excitation coils were supplied in energy by a Kikusui PCR2000WEA power amplifier (Yokohama, Japan) driven by a 33210A Agilent® (Santa Clara, California, USA) arbitrary waveform generator. A 100 Ω resistor was plugged in series with the excitation coils. This resistor was large enough to ensure that the amplifier voltage and current *I(t)* outputs had similar waveforms, whatever the working condition. Another 1 Ω resistor was plugged in series to monitor *I(t)*. Once measured, *I(t)* was used to return $H_{surf}(t)$, according to Eq. 1:

$$\mathrm{H_{surf}(t)} = \frac{2\mathrm{N_t I(t)}}{\mathrm{L_e}} \quad (1)$$

L_e = 27 mm is the length of the specimen in the tested area.

A N_t = 200-turns sensor coil was wrapped around the tested specimens to measure the induced electromagnetic force $Ø(t)$ used to calculate $B_a(t)$ (Eq. 2):

$$\mathrm{B_a(t)} = \frac{1}{\mathrm{N_t S}} \int \emptyset(\mathrm{t})\mathrm{dt} \quad (2)$$

S = 1.95 10^{-5} m^2 is the tested specimen cross-section.

All the signals were recorded with a Dewesoft (Trbovlje, Slovenia) Sirius data acquisition card. Fig. 3 below depicts the whole characterization setup for illustration.

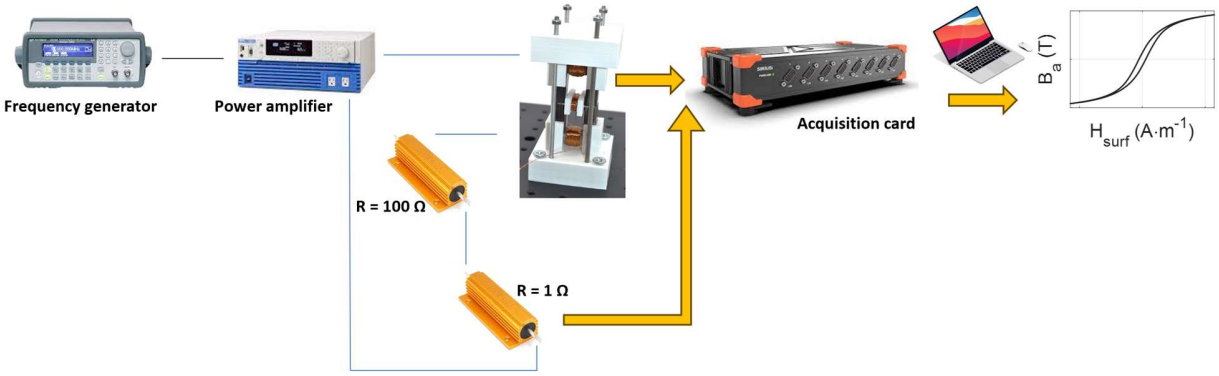

Fig. 3 – Illustration of the complete characterization setup.

4 – Magnetic hysteresis model

Distinct magnetization mechanisms are involved in quasi-static and dynamic conditions, leading to distinct simulation methods [19, 23, 24]. In the very low-frequency range (quasi-static), the skin effect is assumed to be negligible, and the magnetic excitation is homogeneously distributed in the ferromagnetic material. Conversely, eddy currents are generated when the frequency increases, limiting the magnetic field propagation, which becomes heterogeneously distributed.

4.1 – Quasi-static behavior (f << 1 Hz)

The Jiles-Atherton (J-A) ferromagnetic hysteresis model was used to simulate the low-frequency behavior of the tested specimens [25, 26]. This time-independent model was first described in the eighties to simulate soft magnetic laminations under unidirectional magnetization. The J-A model has several advantages:

_ a limited number of parameters,

_ an easy parameter identification through experimental data fitting,

_ its versatility and ability to capture many hysteresis behaviors (major and minor loops, etc.),

_ its simplicity favoring its integration into numerical simulations like finite element analyses.

The magnetization state M in the J-A model is obtained through the incremental resolution of three steps. The first step consists in the calculation of the effective field H_e according to Eq. 3:

$$\mathrm{H_e} = \mathrm{H_{surf}} + \alpha \mathrm{M} \tag{3}$$

where α is the interdomain coupling parameter [25].

$M_{anh,}$ the anhysteretic magnetization is obtained in the second step through the resolution of a sigmoid-type function like the Langevin equation:

$$\mathrm{M_{anh}} = \mathrm{M_s}\left[\coth\left(\frac{\mathrm{H_e}}{\mathrm{a}}\right) - \left(\frac{\mathrm{a}}{\mathrm{H_e}}\right)\right] \tag{4}$$

where M_s is the saturation magnetization and a a parameter quantifying the magnetic domain walls' density. The last step consists of the resolution of the differential equation Eq. 5:

$$\frac{\mathrm{dM}}{\mathrm{dH_{surf}}} = \frac{1}{1+\mathrm{c}}\frac{\mathrm{M_{anh}}-\mathrm{M}}{\delta \mathrm{k}+\alpha(\mathrm{M_{anh}}-\mathrm{M})} + \frac{\mathrm{c}}{1+\mathrm{c}}\frac{\mathrm{dM_{anh}}}{\mathrm{dH_{surf}}} \tag{5}$$

where *c* is a parameter associated with the weight of the magnetization reversibility, *k* with the average energy required to break the pinning sites, and δ = 1 if H_{surf} is increasing and -1 otherwise [25]. *B* and *H* (respectively, the local flux density and magnetic field) are linked to *M* through Eq. 6.

$$\mathrm{B} = \mu_0(\mathrm{H} + \mathrm{M}) \tag{6}$$

In the J-A model's working conditions, *B* and B_a, and *H* and H_{surf} have the same values. Therefore, Eq. 6 is used to return B_a as a function of H_{surf}.

4.2 – Dynamic behavior

The frequency-dependent simulation technique used in this study was constructed based on the approach initially introduced in [27]. This method simultaneously solves the Maxwell diffusion equation (Eq. 7) and a dynamic material law. Considering the specific dimensions of the tested specimens (thickness ζ << width and length), it is feasible to solve Eq. 7 in one dimension (1D) using finite differences while maintaining a good level of precision.

$$\sigma \frac{\partial \mathrm{B}}{\partial \mathrm{t}} = \frac{\partial^2 \mathrm{H}}{\partial \mathrm{z}^2} \tag{7}$$

where σ is the electrical conductivity. For the material law, opting for a straightforward quasi-static hysteresis model, like the J-A model and denoted as $H_{stat}(B)$, is convenient. However, this approach inevitably leads to inaccuracies as it fails to account for the contribution of excess loss. In [25], an enhancement was proposed by introducing a first-order differential equation equivalent to a viscous behavior to improve the accuracy of the material law (Eq. 8):

$$\rho \frac{\mathrm{dB}}{\mathrm{dt}} = \mathrm{H} - \mathrm{H}_{\mathrm{stat}}(\mathrm{B}) \tag{8}$$

Thus, *B* becomes frequency-dependent, and ρ is the unique parameter accounting for this effect. However, this relation was shown to be imprecise, and its applicability was limited to a relatively narrow frequency bandwidth. Subsequently, in [28], an enhancement in the frequency bandwidth was suggested, albeit with additional parameters dependent on *B*. This method works but at the cost of very accurate experimental data. Unfortunately, its predictive capacity is limited, and the simulation settings are poorly transposable. In this work, we chose an alternative solution, which involves a fractional derivative version of the differential equation represented by Eq. 9:

$$\rho \frac{\mathrm{d^n B}}{\mathrm{dt^n}} = \mathrm{H} - \mathrm{H}_{\mathrm{stat}}(\mathrm{B}) \tag{9}$$

Fractional derivative operators balance the dynamic effect distinctly. They provide the simulation method with additional freedom, resulting in precise simulations across broad frequency ranges. ρ in Eq. 9 has a dimension of a resistor if *n* = 1 and a capacitor if *n* = 0. It behaves as a combination of a resistor and a capacitor for non-entire values of *n*.

4.2.1 – Fractional differential equation: physical meaning

Fractional calculus was initially mentioned in the late seventeenth century [29, 30]. In contrast to classical derivatives, fractional derivatives inherently exhibit non-local characteristics. While classical time derivatives describe changes near the current time, fractional derivatives can

capture changes across all the simulated time history. This property is well-suited for ferromagnetic hysteresis, where real-time behavior significantly depends on the material's history. Dynamic in Eq. 8 can be associated with a viscous behavior, but high-speed magnetization in soft ferromagnetic materials is better described through viscoelasticity.

Viscoelasticity is achieved by replacing Eq. 8 with Eq. 9, meaning that magnetization is no longer solely dissipative but elastic, too. In mechanics, viscoelastic models employ combinations of springs and dashpots arranged in series and/or parallel [31, 32]. Springs depict the response of an elastic solid, where stress is proportional to strain (0^{th}-order derivative term). Dashpots represent the response of a viscous fluid, where stress is proportional to the strain rate (1^{st}-order derivative). Using a fractional derivative of order α, where $0 < \alpha < 1$, to model a viscoelastic behavior is grounded in the notion that the actual response lies between that of a 0^{th} and 1^{st}-order derivative, somewhere between an elastic solid and a viscous fluid [32].

The forward Grünwald-Letnikov definition for fractional derivative adheres to the causality principle [33], so we used it in this work:

$$\begin{cases} \mathrm{D}_{\mathrm{f}}^{\mathrm{n}}\mathrm{f}(\mathrm{t}) = \lim\limits_{\mathrm{h}\to 0^{+}} \mathrm{h}^{-\mathrm{n}} \sum_{\mathrm{m}=0}^{\infty} \frac{(-\mathrm{n})_{\mathrm{m}}}{\mathrm{m!}} \mathrm{f}(\mathrm{t}-\mathrm{mh}) \\ (\mathrm{n})_{\mathrm{m}} = \frac{\Gamma(\mathrm{n}+\mathrm{m})}{\Gamma(\mathrm{n})} = \mathrm{m}(\mathrm{m}+1)\dots(\mathrm{n}+\mathrm{m}-1) \\ (\mathrm{m})_0 = 1 \end{cases} \tag{10}$$

($(n)_m$ is the Pochhammer symbol and Γ the gamma function).

4.2.2 – Simultaneous resolution of equations 8 and 10

In [27], the hysteresis problem was solved by a simultaneous resolution of Eq. 7 and 9 through a rewriting in a unique expression constituted of *H* terms exclusively:

$$\frac{\partial^2 \mathrm{H}}{\partial \mathrm{z}^2} = \frac{\mathrm{H}-\mathrm{H}_{\mathrm{stat}}(\mathrm{B})}{\rho} \tag{11}$$

Finite differences were used to solve Eq. 9, leading to a matrix system, including a stiff matrix possibly set in post-processing. The model outputs were the average and local magnetic quantities (H_i(t), B_i(t), and B(t)). This simulation method was straightforward, and the simulation times were limited; therefore, we opted for the same method in this work. Eq. 8 and 9 can be reformulated similarly, but for this, dB/dt has to be isolated in Eq. 9:

$$\frac{\mathrm{d}^{\mathrm{n}}\mathrm{B}}{\mathrm{dt}^{\mathrm{n}}} = \frac{\mathrm{H}-\mathrm{H}_{\mathrm{stat}}(\mathrm{B})}{\rho} \tag{12}$$

$$\frac{\partial \mathrm{B}}{\partial \mathrm{t}} = \frac{\mathrm{d}^{1-\mathrm{n}}\left(\frac{\mathrm{H}-\mathrm{H}_{\mathrm{stat}}(\mathrm{B})}{\rho}\right)}{\mathrm{dt}^{1-\mathrm{n}}} \tag{13}$$

The concatenation of Eq. 7 and 13 leads to Eq. 14:

$$\frac{1}{\sigma}\frac{\partial^2 \mathrm{H}}{\partial \mathrm{z}^2} = \frac{\mathrm{d}^{1-\mathrm{n}}\left(\frac{\mathrm{H}-\mathrm{H}_{\mathrm{stat}}(\mathrm{B})}{\rho}\right)}{\mathrm{dt}^{1-\mathrm{n}}} \tag{14}$$

Here again, finite differences can be applied to the left term and Eq. 10's fractional derivative definition to the right one [34]. The resulting equation becomes exclusively constituted of *H* terms:

$$\frac{H(z-r,t)-2\ (z,t)+H(z+r,t)}{r^2} = \sigma \lim_{h\to 0^+} h^{n-1} \cdot \sum_{m=0}^{\infty} \frac{(n-1)_m}{m!} \left(\frac{H(z,t-mh)-H_{stat}(B(z,t-mh))}{\rho} \right) \quad (15)$$

Since $H(z,t)$ and $B(z,t)$ are symmetric about the plane $z = \zeta/2$, a resolution on the segment $[0, \zeta / 2]$ is enough, and a Neumann condition can be applied to the $z = \zeta/2$ node (see Fig. 4 for illustration). In this condition, r the space discretization (Eq. 12) is worth $\zeta/[2(N-1)]$, and N is the number of nodes.

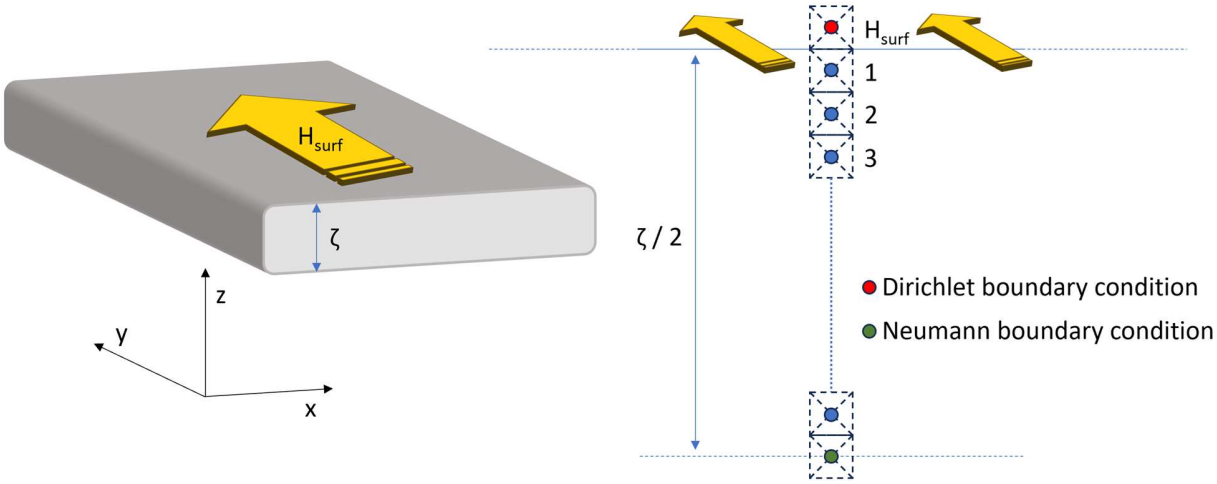

Fig. 4 – Illustration for the 1D space discretization resolution scheme, including the boundary conditions.

The spatial resolution of Eq. 12 leads to a matrix system Eq. 17:

$$[A].[H] = [S] \quad (16)$$

where [A] is the stiffness matrix, which can be computed during a pre-processing stage and kept unchanged for the entire simulation. Conversely, the matrix system needs to be solved at each simulation step. This resolution yields the discretized excitation field H_i. It is followed by localized resolutions of Eq. 9, resulting in B_i. In the final stage, B_a is determined by averaging the local induction:

$$B_a = \frac{\sum_{i=1}^{N} B_i}{N} \quad (17)$$

When plotted against H_{surf}, the resulting simulated hysteresis cycle $H_{surf}(B_a)$ can be compared with its experimental counterpart. The Derivative Static Hysteresis Model (DSHM) was used as $H_{stat}(B_a)$ to enhance the simulation times and streamline memory management. This method is described in references [35, 36]. It relies on a 2D interpolation matrix, where columns and rows represent discrete values of static H_{surf} and static B_a, and the matrix elements indicate the dB_a/dH_{surf} slope at the corresponding point. As mentioned in [34], DSHM can easily switch from H_{surf} to B_a-imposed input conditions. To fulfill the DSHM matrix, experimental first-order reversal curves are typically utilized, although obtaining such experimental data can be challenging. In this study, we substituted them with simulated first-order reversal curves generated using the J-A model [25, 26].

5 – Comparison simulations/measurements

5.1 – Quasi-static behavior

5.1.1 – Virgin and fully dealloyed specimens

The first comparison simulations/measurements, shown in Fig. 5, concerns virgin and fully-dealloyed specimens. Experimental tests were performed under a sinus-shape H_{surf} of amplitude 1.15 x 10^4 A·m^{-1} and a frequency of 0.1 Hz. The simulation parameters giving the best fit are shown in Table 1. Although studies describing how these parameters can be obtained through theoretical methods exist in the literature [26], they were tested and found to have limited accuracy. In this work, where accuracy is a major factor and simulation time is not a limitation, we opted for a numerical method instead. Therefore, the simulation parameters were obtained using an optimization process consisting of minimizing the relative Euclidean distance criteria by comparing a simulated and an experimental hysteresis cycle (RED(%), Eq. 18) [37] (where q is the number of experimental discretizations used to describe the hysteresis cycle). At the beginning of the iteration, a large window of values is set for each parameter. These windows are gradually reduced as the optimization process progresses. Eventually, the combination of parameters that gives the lowest RED(%) value is conserved and attributed to the tested material. Matlab® needs approximately 10 seconds to test 10,000 combinations. By assigning 20 values to each parameter, a maximum of 53 minutes is required to test all possible combinations.

$$\mathrm{RED}(\%) = \frac{100}{q} \cdot \sum_{i=1}^{q} \frac{\sqrt{\left(Ba_{meas_i}\left(H_{surf_i}\right) - Ba_{sim_i}\left(H_{surf_i}\right)\right)^2}}{\sqrt{\left(Ba_{meas_i}\left(H_{surf_i}\right)\right)^2}} \tag{18}$$

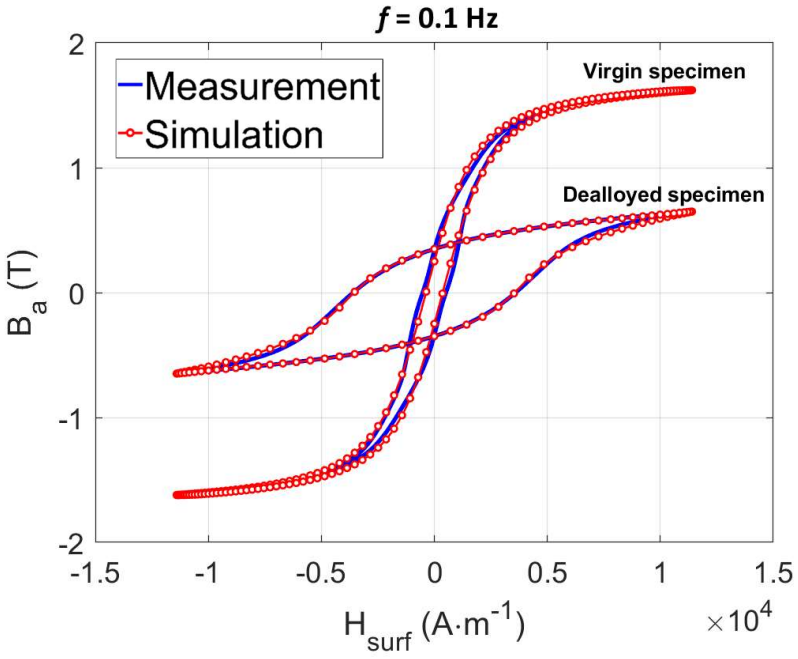

Fig. 5 – Comparison simulations/measurements for the $B_a(H_{surf})$ curve of the virgin and fully-dealloyed specimens *at* f = 0.1 Hz.

The RED(%) was 8.29 for the virgin specimen and 4.38 for the fully-dealloyed one, respectively.

5.1.2 – Partially dealloyed specimen

In quasi-static conditions, H is homogeneously distributed in the specimen and supposedly equal to H_{surf}. The distinct layers of the partially-dealloyed specimens can be simulated separately, considering both under the influence of H_{surf} and using the simulation method and parameters set in sub-section 5.1.1. Then, B_a is calculated in post-processing by solving Eq. 19 (similar to a rule of mixture):

$$\mathrm{B_a} = \upsilon \mathrm{B_{aV}} + (1-\upsilon)\mathrm{B_{aD}} \tag{19}$$

B_{aV} and B_{aD} represent the average flux density of the virgin and dealloyed layers, respectively, and $\upsilon = th_V/th_D$ is the ratio between their thicknesses. υ is considered unknown to reproduce the working conditions of a non-destructive evaluation. It becomes a degree of freedom in the simulation process, which can be obtained through the previously described optimization process.

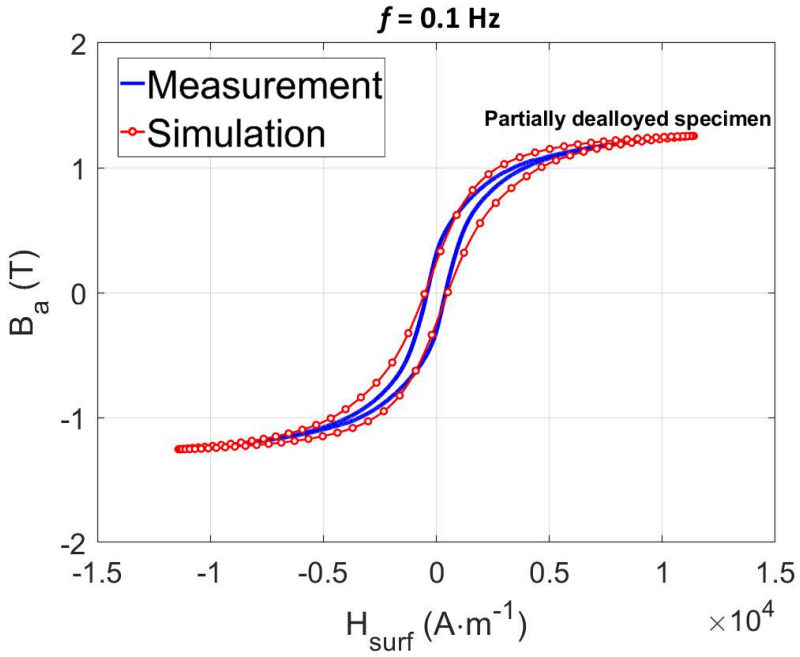

Fig. 6 – Comparison simulation/measurement for the $B_a(H_{surf})$ curve of the partially-dealloyed specimens *at* f = 0.1 Hz.

The optimization process gave RED(%) = 9.2 for υ = 0.721, which means a predicted thickness of the dealloyed layer close to 182 µm. A higher discrepancy is visible in the simulated curve of Fig. 6 near the saturation elbow. The J-A model simplifies the complex interactions between magnetic domains within a material. Near the saturation elbow, these interactions can become particularly intricate and may not be fully accounted for by the model's assumptions.

5.2 – Dynamic behavior

5.2.1 – Virgin and fully dealloyed specimens

The frequency-dependent parameters (ρ, n) for the virgin and fully-dealloyed specimens were obtained through the same optimization process. However, the experimental data were those of the hysteresis cycles obtained at higher frequencies (f = 1, 10, and 100 Hz). Fig. 7 shows the comparisons simulation/measurement in these conditions. The RED% were 3.8 and 2.8 for the virgin and the fully-dealloyed specimens, respectively. The electrical conductivities used for the simulation are given in Table 1. They were measured using the four-point probe method as described in [13]. The presence of pores in the fully-dealloyed specimen drastically reduces this electrical conductivity.

Table 1 – Simulation parameters and physical properties of the virgin and fully dealloyed specimens.

J-A static hysteresis model parameters:

	Virgin specimen	Fully dealloyed specimen
M_s ($A \cdot m^{-1}$)	1380000	620000
a ($A \cdot m^{-1}$)	810	9240
k ($A \cdot m^{-1}$)	450	4020
c	0.15	0.005
α	$2\ 10^{-7}$	0.039

Dynamic model parameters:

n	0.98	0.99
ρ	7.9	12.5

Material property:

σ ($S \cdot m^{-1}$)	$1.22\ 10^{7}$	$6.135\ 10^{5}$

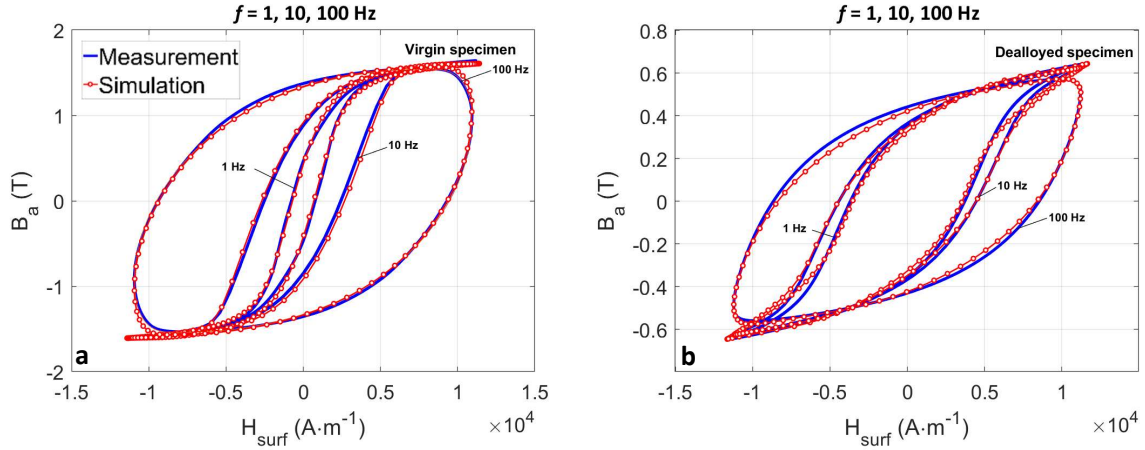

Fig. 7 – a Comparison simulations/measurements for the $B_a(H_{surf})$ curves of the virgin specimens at f = 1, 10, and 100 Hz. **Fig. 7 – b** Same comparison for the fully dealloyed specimens.

5.2.2 – Partially dealloyed specimen

Adapting the dynamic hysteresis model to the partially-dealloyed specimens is straightforward. For this, we assume the thickness of the transition layer is negligible and the boundary between the dealloyed and the virgin layer is a planar front. This reasonable assumption leads to an optimization process including a single degree of freedom corresponding to the thickness of the dealloyed layer. The finite differences nodes located in the dealloyed layer are simulated with the material properties of the fully-dealloyed specimen (static hysteresis contribution, n, ρ, and σ), and the nodes located in the virgin layer with those of the virgin one (Fig. 8). The optimization process is based on the same principle (minimization of the RED% (Eq. 16) by comparing simulations and measurements). 20 nodes were enough to simulate precisely

the virgin and fully-dealloyed specimens, but 160 nodes were necessary to accurately estimate the dealloyed layer's thickness.

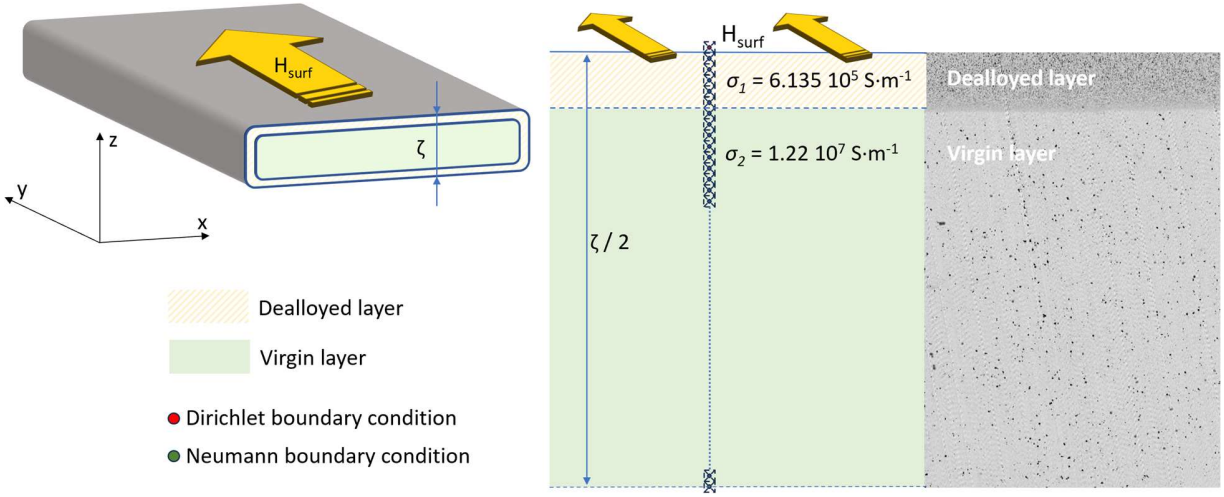

Fig. 8 – Illustration of the simulation process for the partially dealloyed specimens.

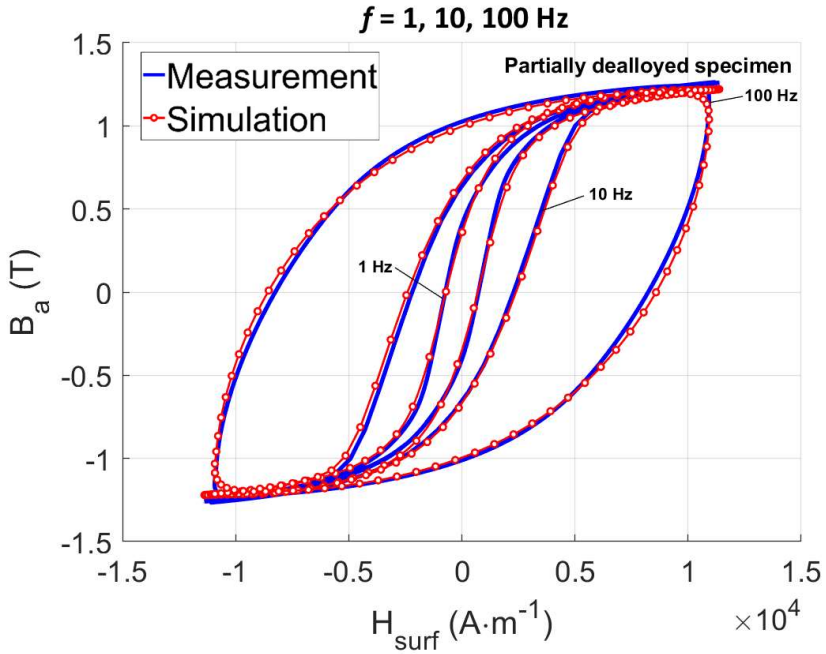

Fig. 9 – Comparison simulations/measurements for the partially dealloyed specimens and for f = 1, 10, and 100Hz.

Finally, for the partially-dealloyed specimens, the best simulation results (RED% = 7.42) were obtained with the nodes {1-24} configurated with the fully-dealloyed parameters, which correspond to a predicted thickness of 195 µm for the dealloyed layer. All available dynamic

experimental results (f = 1, 10, and 100 Hz) were used as the data set in the optimization process. Fig. 9 shows the hysteresis cycle comparisons for the partially-dealloyed specimen.

5.3 – Discussion

The SEM image in Fig. 10 confirmed the planar nature of the dealloying front, thereby justifying the models' assumptions. It revealed a dealloyed layer thickness of approximately 181 µm, resulting in a 0.5% error for the static hysteresis model prediction and a 7.7% error for the dynamic one. Despite the static model displaying higher accuracy, with predictive errors below 10%, both methods can be considered validated.

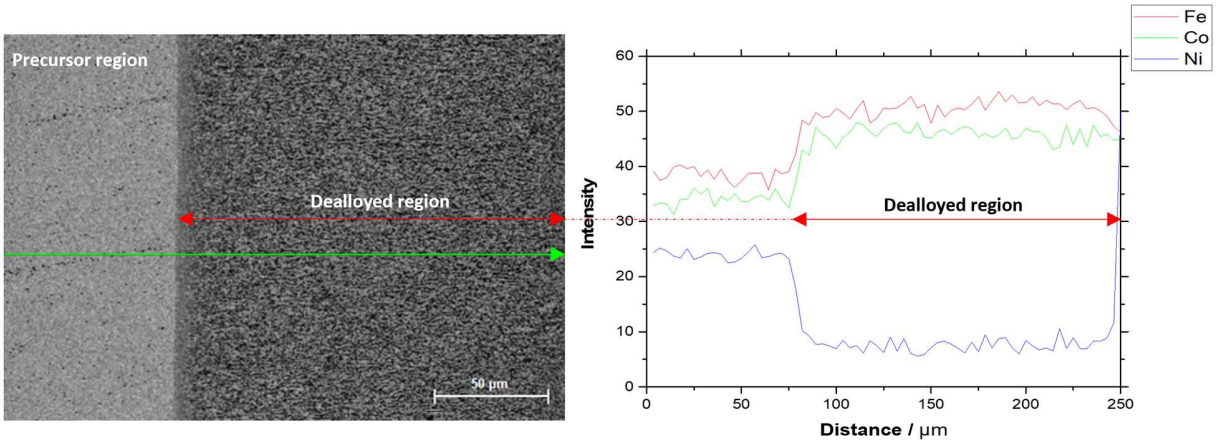

Fig. 10 – Precise measurement of the dealloyed layer thickness from FE-SEM image.

To better illustrate the difference in magnetic properties between the bulk porous regions of the specimens, we generated numerically a connected porous structure with the porosity of the fully dealloyed layer from a phase field model for spinodal decomposition [38]. Such a model allows to generate connected random bicontinuous microstructures that can be considered proxies for the microstructures obtained from LMD [39, 40]. In particular, we generated a 8 × 8 × 8 µm^3 volume with a porosity of 30% that is representative of the dealloyed microstructure. The resulting volume was imported into Comsol Multiphysics 6.0 (Stockholm, Sweden). FeCo alloy and air magnetic properties were used for the metallic and the pores phases, respectively.

The dealloying process strongly impacts the magnetic properties. The flux density levels are, as an example, divided by more than two in the experimental results of Fig. 5. This decrease is partly associated with the evolution of the specimen porosity, which, according to [13], reaches nearly 30% for a complete dealloyed process in the conditions of this study. Even if the material dimensions are unchanged, the effective cross-section is reduced significantly. Still, this property is not considered in Eq. 2 to convert the electromotive force into a flux density. In the finite element simulation, a significant difference (≈ 31 %) can be observed between the effective cross-section of the original specimen and the dealloyed one (red zone in Fig. 11 – b). Another explanation for the decrease in flux density is also associated with the presence of pores. These small volumes of non-ferromagnetic properties inside the specimen modify the trajectory of the magnetic line (Fig. 11 – c). The distance traveled by the magnetic field increases significantly,

which reduces its overall local magnitude. For the same level of H_{surf}, a significative saturation is obtained for the virgin specimen's f = 0.1 Hz curve, but it is far from the case for the fully-dealloyed specimen (Fig. 5).

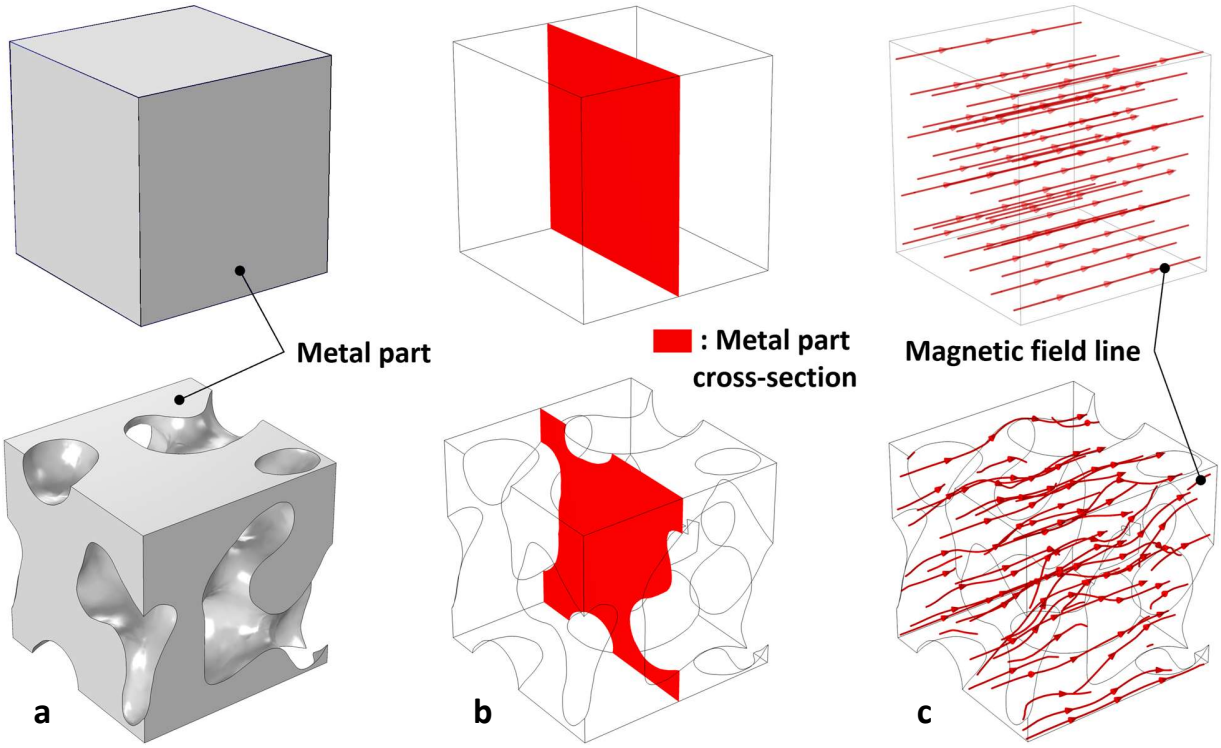

Fig. 11 – Illustration for the FEM simulation of a representative volume of the fully dealloyed layer. **Fig. 11 – a** Comparison between the virgin and fully-dealloyed geometry. **Fig. 11 – b** Same comparison for the metal cross-section. **Fig. 11 – c** Same comparison for the magnetic field line.

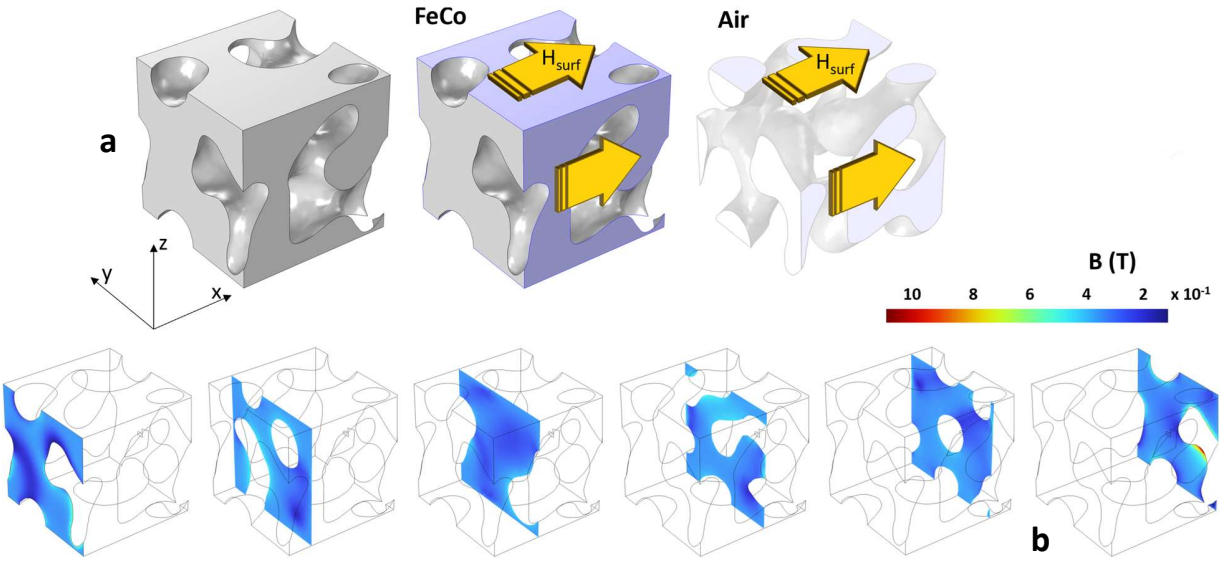

Fig. 12 – FEM simulation results of a representative volume of the fully dealloyed layer. **Fig. 12 – a** Illustration of the boundary conditions. **Fig. 12 – b** Magnetic flux density in various yz-cross-sections.

This explanation also partly justifies the difference in coercivity (Fig. 13) in the quasi-static regime (more than six times larger for the dealloyed specimen than the virgin one). However, the difference in the trajectory of the magnetic lines between the virgin and the fully-dealloyed specimen (Fig. 11 – c) is clearly not in the same ratio, and another phenomenon must be happening to justify such a difference.

The effect of residual stress on the magnetic behavior of FeCo alloys is noteworthy and may offer a plausible explanation [41]. The Mg phase thermal expansion coefficient is larger than the FeCo's, and a significant thermal strain is induced during solidification. By increasing the porosity and etching the Mg phase, LMD is expected to release stress, if any, yet the subsequent 12-hour heat treatment post-cold-rolling also serves this purpose. Therefore, the virgin specimens are expected to be free of stress. Preliminary X-ray diffraction tests confirmed the absence of residual stress, thereby refuting this explanation.

A secondary effect lies in the presence of magnetic line concentrators. Together with the nonlinear magnetic behavior of the FeCo material, they induce local magnetic hot spots, which reduces the overall magnetic permeability of the metallic phase and leads to the need for higher levels of magnetic fields for similar magnetization states. These magnetic hot spots are observable in Fig. 12 – b, which is obtained by imposing H_{surf} = 2000 A·m^{-1} on the lateral sides of the representative volume.

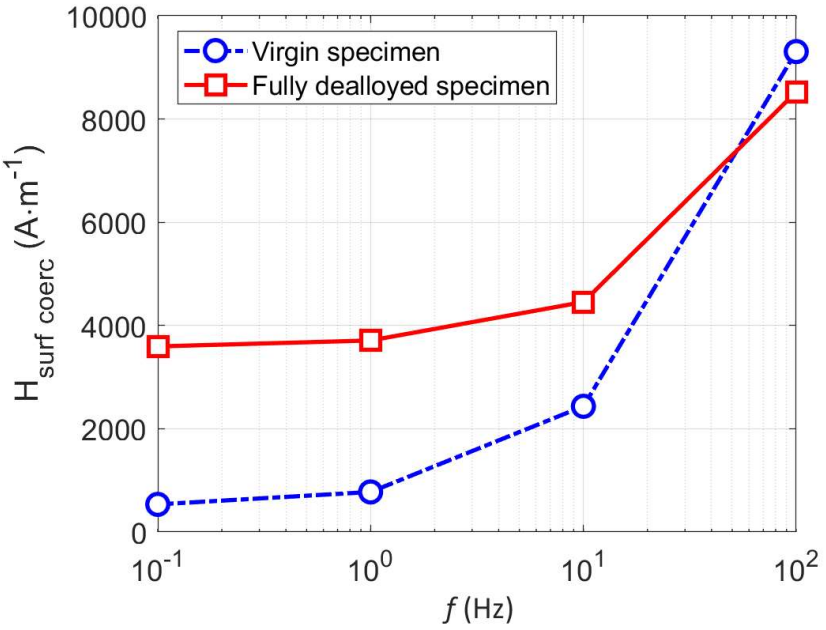

Fig. 13 – Variation of the coercivity versus frequency.

Coercivity is known to be ruled by fundamental interplay between material constants in bulk magnetic alloys [42]. In Fig. 13, the reduction of the coercivity differences when the frequency increases is worth noting ($\Delta H_{surfc}/df > 17$ between 0.1 Hz and 100 Hz for the virgin specimen and only $dH_{surfc}/df < 2.4$ for the fully-dealloyed one). This reduction is due to the difference in electrical conductivity and the significantly lower level of eddy currents in the dealloyed specimen. This observation somehow reflects the frequency dependency of the magnetic losses.

The good simulation results obtained with n close to 1 denote a substantial contribution of the viscous behavior of the domain wall motions and the low impact of the excess loss for the levels of frequency tested. Such a property for FeCo alloys has already been observed, like in Fig. 6 of [43], where the excess loss contribution is about ten times lower than the hysteresis one and significantly lower than the classic one. The reduced difference between the optimal values of n obtained for the virgin and fully dealloyed specimens denotes that the disparity observed between the experimental measurements can primarily be attributed to ρ. The significant difference between the optimal ρ given in Table 1 confirms this observation.

6 – Conclusion

Surface treatments are recommended to improve the physical properties of metallic parts' top layers. When it comes to magnetic properties, it has, for instance, already been demonstrated that silicon diffusion can significantly enhance the surface magnetic properties of electrical steel laminations [8-10, 44, 45]. This process modifies the surface resistivity while maintaining good mechanical properties for the unaffected inner layers.

In this work, we have investigated the magnetic properties of specimens treated through a liquid metal dealloying process. The treated specimens exhibit reduced surface electrical conductivity, so they are anticipated to handle the frequency effects better and demonstrate diminished magnetic loss.

The magnetic hysteresis cycles of virgin, fully-dealloyed, and partially-dealloyed specimens were measured and plotted under various frequencies of magnetic excitation. Subsequently, hysteresis models were set up to replicate these cycles in both quasi-static and dynamic scenarios. The simulation parameters from fully-dealloyed and virgin specimens were employed to predict the behavior of partially-dealloyed specimens and accurately and non-destructively estimate the treated area's thickness. The numerical predictions were confronted with the actual thickness measurements obtained with SEM measurements, and shallow error levels were obtained (RED(%)< 8%).

Then, a finite element simulation was designed to simulate a 3D representative volume of the dealloyed layer. The overall simulation results suggest that the porosity minimally affects the magnetic behavior of the metallic part, and the observed variations are primarily attributed to the distortion of the magnetic lines and changes in local geometry.

This study focused on the magnetic property of the LMD-treated specimens, but future works could complement it with mechanical investigation. The coupling properties (magnetostriction, Villari effect) have not been studied as well, even if the impact of a multi-phase presence in a metallic structure on these properties has already been demonstrated to be significant [46].

Finally, even if the LMD treatment reduces the electrical conductivity and the resulting frequency effect is less impactful, the magnetic behavior is unfortunately also affected (higher coercivity, lower magnetization saturation, etc.), and so should be the mechanical properties. The impact of the porosity level has not been observed nor discussed in this paper, but it will obviously modify the overall magnetic behavior.

Eventually, as is usually the case for surface treatments, a compromise between magnetic loss, permeability, saturation level, and mechanical properties will have to be set regarding the actual targeted application. This compromise will assess the level of porosity and the thickness of the treated layer.

The dealloyed layer's magnetic properties significantly depend on the microstructure (ligament size, composition, porosity rate, etc.), and LMD provides a way to optimize these properties, which consists in another exciting prospect of this work. Controlling LMD microstructure orientation could also potentially yield assertive anisotropic magnetic behavior.

References

[1] Wada, T., Geslin, P.A., Wei, D. and Kato, H., 2023. Partial liquid metal dealloying to synthesize nickel-containing porous and composite ferrous and high-entropy alloys. *Communications Materials*, *4*(1), p.43.

[2] Joo, S.H., Wada, T. and Kato, H., 2019. Development of porous FeCo by liquid metal dealloying: Evolution of porous morphology and effect of interaction between ligaments and melt. *Materials & Design*, *180*, p.107908.

[3] Guo, X., Zhang, C., Tian, Q. and Yu, D., 2021. Liquid metals dealloying as a general approach for the selective extraction of metals and the fabrication of nanoporous metals: A review. *Materials Today Communications*, *26*, p.102007.

[4] Geslin, P.A., McCue, I., Gaskey, B., Erlebacher, J. and Karma, A., 2015. Topology-generating interfacial pattern formation during liquid metal dealloying. *Nature communications*, *6*(1), p.8887.

[5] McCue, I., Benn, E., Gaskey, B. and Erlebacher, J., 2016. Dealloying and dealloyed materials. *Annual review of materials research*, *46*, pp.263-286.

[6] McCue, I., Gaskey, B., Geslin, P.A., Karma, A. and Erlebacher, J., 2016. Kinetics and morphological evolution of liquid metal dealloying. *Acta Materialia*, *115*, pp.10-23.

[7] Kim, J.W., Tsuda, M., Wada, T., Yubuta, K., Kim, S.G. and Kato, H., 2015. Optimizing niobium dealloying with metallic melt to fabricate porous structure for electrolytic capacitors. *Acta Materialia*, *84*, pp.497-505.

[8] Kim, J.W., Wada, T., Kim, S.G. and Kato, H., 2016. Enlarging the surface area of an electrolytic capacitor of porous niobium by MgCe eutectic liquid dealloying. *Scripta Materialia*, *122*, pp.68-71.

[9] De Lacheisserie, E.D.T., Gignoux, D. and Schlenker, M. eds., 2012. *Magnetism: II-Materials and Applications*. Springer Science & Business Media.

[10] Kasai, S., Namikawa, M. and Hiratani, T., 2016. Recent progress of high silicon electrical steel in JFE steel. *JFE Tech. Rep*, *21*(03), pp.14-19.

[11] Ros-Yáñez, T., Ruiz, D., Barros, J. and Houbaert, Y., 2004. Advances in the production of high-silicon electrical steel by thermomechanical processing and by immersion and diffusion annealing. *Journal of alloys and compounds*, *369*(1-2), pp.125-130.

[12] Hiratani, T., Zaizen, Y., Oda, Y., Yoshizaki, S. and Senda, K., 2018. Investigation of the magnetic properties of Si-gradient steel sheet by comparison with 6.5% Si steel sheet. *AIP Advances*, *8*(5).

[13] Joo, S.H. and Kato, H., 2022. 3D interconnected nanoporous FeCo soft magnetic materials synthesized by liquid metal dealloying. *Journal of Alloys and Compounds*, *908*, p.164688.

[14] Sourmail, T., 2005. Near equiatomic FeCo alloys: Constitution, mechanical and magnetic properties. *Progress in Materials Science*, *50*(7), pp.816-880.

[15] Sundar, R.S. and Deevi, S.C., 2005. Soft magnetic FeCo alloys: alloy development, processing, and properties. *International materials reviews*, *50*(3), pp.157-192.

[16] Jiles, D.C., 2003. Recent advances and future directions in magnetic materials. *Acta materialia*, *51*(19), pp.5907-5939.

[17] Sheykholeslami, M., Hojjat, Y., Ghodsi, M., Zeighami, M. and Kakavand, K., 2016. Effect of magnetic field on mechanical properties in Permendur. *Materials Science and Engineering: A*, *651*, pp.598-603.

[18] Bloch, F., Waeckerle, T. and Fraisse, H., 2007, October. The use of iron-nickel and iron-cobalt alloys in electrical engineering, and especially for electrical motors. In *2007 Electrical Insulation Conference and Electrical Manufacturing Expo* (pp. 394-401). IEEE.

[19] Fiorillo, F., Bertotti, G., Appino, C. and Pasquale, M., 2016. Soft magnetic materials. In *Wiley Encyclopedia of Electrical and Electronics Engineering* (pp. 1-42). John Wiley & Sons, Inc..

[20] Ducharne, B., Sebald, G., Guyomar, D. and Litak, G., 2015. Dynamics of magnetic field penetration into soft ferromagnets. *Journal of Applied Physics*, *117*(24).

[21] Ducharne, B., Tsafack, P., Deffo, Y.T., Zhang, B. and Sebald, G., 2021. Anomalous fractional magnetic field diffusion through cross-section of a massive toroidal ferromagnetic core. *Communications in Nonlinear Science and Numerical Simulation*, *92*, p.105450.

[22] Ducharne, B., Hamzehbamani, H., Gao, Y., Fagan, P., Sebald, G., 2024. High-frequency fractional predictions and spatial distribution of the magnetic loss in a grain-oriented magnetic steel lamination, *fractal and fractional*, under review.

[23] Mörée, G. and Leijon, M., 2023. Review of Hysteresis Models for Magnetic Materials. *Energies*, *16*(9), p.3908.

[24] Ivanyi, A., 1997. Hysteresis models in electromagnetic computation" col. *A, Budapest pp 92*, *114*.

[25] Jiles, D., 2015. *Introduction to magnetism and magnetic materials*. CRC press.

[26] Jiles, D.C. and Atherton, D.L., 1984. Theory of ferromagnetic hysteresis. *Journal of applied physics*, *55*(6), pp.2115-2120.

[27] Raulet, M.A., Ducharne, B., Masson, J.P. and Bayada, G., 2004. The magnetic field diffusion equation including dynamic hysteresis: a linear formulation of the problem. *IEEE transactions on magnetics*, *40*(2), pp.872-875.

[28] Zirka, S.E., Moroz, Y.I., Marketos, P. and Moses, A.J., 2005. A viscous-type dynamic hysteresis model as a tool for loss separation in conducting ferromagnetic laminations. *IEEE transactions on magnetics*, *41*(3), pp.1109-1111.

[29] Machado, J.T., Kiryakova, V. and Mainardi, F., 2011. Recent history of fractional calculus. *Communications in nonlinear science and numerical simulation*, *16*(3), pp.1140-1153.

[30] Butzer, P.L. and Westphal, U., 2000. An introduction to fractional calculus. In *Applications of fractional calculus in physics* (pp. 1-85).

[31] Findley, W.N. and Davis, F.A., 2013. *Creep and relaxation of nonlinear viscoelastic materials*. Courier corporation.

[32] Bonfanti, A., Kaplan, J.L., Charras, G. and Kabla, A., 2020. Fractional viscoelastic models for power-law materials. *Soft Matter*, *16*(26), pp.6002-6020.

[33] Ortigueira, M. and Machado, J., 2017. Which derivative?. *Fractal and Fractional*, *1*(1), p.3.

[34] Ducharne, B. and Sebald, G., 2022. Combining a fractional diffusion equation and a fractional viscosity-based magneto dynamic model to simulate the ferromagnetic hysteresis losses. *AIP Advances*, *12*(3).

[35] Scorretti, R., Sabariego, R.V., Sixdenier, F., Ducharne, B. and Raulet, M.A., 2011, July. Integration of a new hysteresis model in the Finite Elements method. In *Compumag 2011* (pp. n-334).

[36] Fagan, P., Ducharne, B. and Skarlatos, A., 2021, April. Optimized magnetic hysteresis management in numerical electromagnetic field simulations. In *2021 IEEE International Magnetic Conference (INTERMAG)* (pp. 1-5). IEEE.

[37] Fagan, P., Ducharne, B., Zurek, S., Domenjoud, M., Skarlatos, A., Daniel, L. and Reboud, C., 2022. Iterative methods for waveform control in magnetic measurement systems. *IEEE Transactions on Instrumentation and Measurement*, *71*, pp.1-13.

[38] Kwon, Y., Thornton, K. and Voorhees, P.W., 2009. The topology and morphology of bicontinuous interfaces during coarsening. *Europhysics Letters*, *86*(4), p.46005.

[39] Geslin, P.A., Buchet, M., Wada, T. and Kato, H., 2019. Phase-field investigation of the coarsening of porous structures by surface diffusion. *Physical Review Materials*, *3*(8), p.083401.

[40] Okulov, I.V., Geslin, P.A., Soldatov, I.V., Ovri, H., Joo, S.H. and Kato, H., 2019. Anomalously low modulus of the interpenetrating-phase composite of Fe and Mg obtained by liquid metal dealloying. *Scripta Materialia*, *163*, pp.133-136.

[41] Sheykholeslami, M., Hojjat, Y., Ghodsi, M., Zeighami, M. and Kakavand, K., 2016. Effect of magnetic field on mechanical properties in Permendur. *Materials Science and Engineering: A*, *651*, pp.598-603.

[42] Balakrishna, A.R. and James, R.D., 2021. A tool to predict coercivity in magnetic materials. *Acta Materialia*, *208*, p.116697.

[43] Banu, N., Ferrara, E., Pasquale, M., Fiorillo, F., De la Barrière, O., Brunt, D., Wilson, A. and Harmon, S., 2023. Temperature and frequency dependence of magnetic losses in Fe-Co. *IEEE Access*.

[44] Wu, J., Zhang, L., Gong, T., Zhu, J., Hao, Q., Qin, Z., Cong, S., Zhan, D. and Xiang, Z., 2015. Texture evolution of the surface layer of high silicon gradient electrical steel and influence on the magnetic properties. *Vacuum*, *119*, pp.189-195.

[45] Chen, J., Zhao, W., Zheng, X., Lu, R., Guo, C., Chen, S., Du, J., Yu, C. and Liu, X., 2023. High-performance gradient Fe-Si alloy thin sheets fabricated by solid powder siliconizing and diffusion annealing. *Journal of Alloys and Compounds*, *946*, p.169412.

[46] Meng, C., Wang, H., Wu, Y., Liu, J. and Jiang, C., 2016. Investigating enhanced mechanical properties in dual-phase Fe-Ga-Tb alloys. *Scientific Reports*, *6*(1), p.34258.